Volume 1 | Number 1 | Jan 2013 | Pages 1–100

Journal of
Materials Chemistry A

Materials for energy and sustainability
www.rsc.org/materialsA

ROYAL SOCIETY
OF CHEMISTRY

This is an *Accepted Manuscript*, which has been through the Royal Society of Chemistry peer review process and has been accepted for publication.

Accepted Manuscripts are published online shortly after acceptance, before technical editing, formatting and proof reading. Using this free service, authors can make their results available to the community, in citable form, before we publish the edited article. We will replace this *Accepted Manuscript* with the edited and formatted *Advance Article* as soon as it is available.

You can find more information about *Accepted Manuscripts* in the **Information for Authors**.

Please note that technical editing may introduce minor changes to the text and/or graphics, which may alter content. The journal's standard **Terms & Conditions** and the **Ethical guidelines** still apply. In no event shall the Royal Society of Chemistry be held responsible for any errors or omissions in this *Accepted Manuscript* or any consequences arising from the use of any information it contains.

ROYAL SOCIETY
OF CHEMISTRY

www.rsc.org/materialsA

Environmental SEM monitoring of $Ce_{1-x}Ln_xO_{2-x/2}$ mixed-oxides microstructural evolution during dissolution.

D. Horlait, L. Claparede , F. Tocino, N. Clavier, J. Ravaux, S. Szenknect, R.

5 **Podor and N. Dacheux**[*]

ICSM-UMR5257 CNRS/CEA/UM2/ENCSM, Site de Marcoule, Bat. 426, BP 17171, 30207 Bagnols/Cèze, France

10 [*] Contact Author: Tel: +33466339205; E-mail: nicolas.dacheux@univ-montp2.fr

TOC
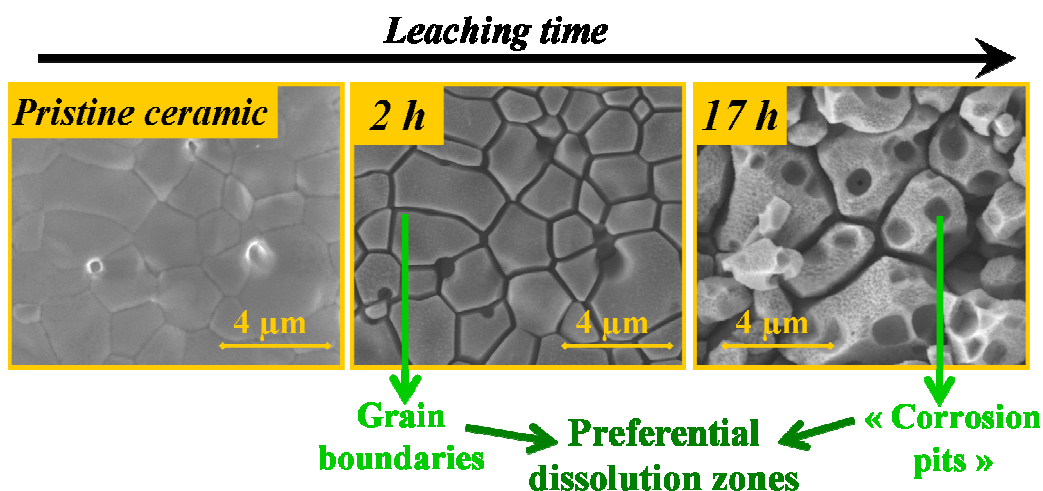
15

Evolution of sintered $Ce_{1-x}Ln_xO_{2-x/2}$ samples during dissolution tests in acidic media was followed on the same zone by environmental scanning microscopy.

20

Abstract

The microstructural evolution of several $Ce_{1-x}Ln_xO_{2-x/2}$ (Ln = Nd, Er, x = 0.28; 0.59 and 0.76) sintered pellets was studied during their dissolution in 4M HNO_3 at 90°C or 60°C. Environmental Scanning Electron Microscopy (ESEM) experiments were developed to follow the changes in the samples microstructure and their consequences on the dissolution evolution by monitoring a constant zone of the material throughout the alteration process. The Ln^{III} content was the parameter affecting the most the dissolution kinetics of such solid solutions. From a microstructural point of view, grain boundaries dissolve preferentially during the first dissolution step due to their relative weakness compared to the well-crystallized bulk material. Crystal defects, namely screw and edge dislocations, constitute the second kind of preferential dissolution zone and induce the formation and growth of corrosion pits, mainly of pyramidal shape on the whole surface. Both microstructural parameters are responsible for significant and non-linear increase of the reactive surface developed at the solid/liquid interface and thus important modifications of the topology. On sintered samples and even more clearly on powdered $Ce_{0.72}Nd_{0.28}O_{1.86}$ sample, the formation of a gelatinous layer resulting of processes occurring in the back-end of the dissolution process (*e.g.* local saturation of the leaching solution), was evidenced through ESEM observations. This gel is also presumably responsible for the progressive decrease of the normalized dissolution rate. From these observations, it appears that the study of a material dissolution kinetics can clearly benefit from the monitoring of the microstructure evolution and particularly that of reactive surface area during dissolution.

A Introduction

During the last two decades, several new concepts of nuclear reactors[1-7] using various kind of fuels[8] have emerged, especially in the frame of GenIV international forum[9]. Whether the considered cycle lays on the direct geological repository of the spent fuel or on its reprocessing, the dissolution
5 behaviors of the foreseen fuels have to be precisely assessed and understood. However, the chemical durability under leaching conditions of spent fuels remains insufficiently apprehended up to now, even for the actual common oxides fuels. In particular, the relative specific influence of the numerous different dissolution parameters (leaching media, spent fuel composition and homogeneity, presence of additional phases, radiation damage, etc.) and of the fuel history (burnup, microstructural evolution
10 during irradiation in reactor, etc.) are poorly known. In order to give a first insight of the role of several parameters on the dissolution kinetics, leaching experiments were conducted on several surrogates of oxide nuclear fuels of the type $M_{1-x}M'_xO_2$ where M and M' correspond to Ce, Th or U, and $M_{1-x}M''_xO_{2-x/2}$ where M'' stands for trivalent lanthanide element[10-17]. In this context, the particular influence of well identified parameters such as temperature, acidity and the leaching solution
15 composition was examined[10-15]. Meanwhile, others associated to the material microstructure, including crystallite size, grain size, cation homogeneity were examined for the first time on powdered samples[16,17].

The present work deals with the investigations on sintered materials mainly focusing on the influence of microstructural characteristics of the ceramics. It takes advantage on the use of
20 environmental scanning electron microscopy (ESEM) for making the observations of the samples microstructure evolutions during dissolution experiments. In this field, dissolution of $Ce_{1-x}Ln_xO_{2-x/2}$ model mixed-oxides (Ln = Nd or Er) were conducted in 4M HNO_3. It is clear that cerium-based oxides appear as a simplified model of tetravalent actinides oxides (such as uranium, neptunium, plutonium) during dissolution, without any redox reactions that could be developed at the solid/liquid interface in
25 oxidizing conditions. However, Ce^{+IV} is often considered as a convenient surrogate for tetravalent actinides (Th, U, Pu)[18], while the behavior of trivalent actinides or fission products was examined from that of neodymium. The dissolution experiments monitored by ESEM were first performed at 90°C on $Ce_{0.72}Nd_{0.28}O_{1.86}$ and $Ce_{0.71}Er_{0.29}O_{1.855}$ sintered pellets in order to assess the influence of the nature of trivalent lanthanide. It was then focused on the results obtained during the dissolution of
30 $Ce_{0.41}Nd_{0.59}O_{1.705}$ pellet at 60°C in order to better examine more advanced dissolution mechanisms as well as to study the own influence of trivalent element content. The results were finally compared to that obtained on a polyphase system ($Ce_{0.24}Nd_{0.76}O_{1.62}$) and on $Ce_{0.72}Nd_{0.28}O_{1.86}$ reactive powder.

B Experimental

$Ce_{0.72}Er_{0.28}O_{1.86}$ and $Ce_{1-x}Nd_xO_{2-x/2}$ (x = 0.29 ; 0.59 and 0.76) dense pellets, whose compositions and other characteristics are gathered in Table 1, were prepared by sintering from the starting powdered mixed-oxides as already described in the literature[10-13]. They were obtained by calcination of mixed-oxalate precursors which starting reactivity was enhanced through manual grinding. They were then compacted by an uniaxial press with a pressure of about 100 MPa to form cylindrical pellets (diameter ≈ 1 cm). These latter were heated in alumina boats up to 1400°C for 10 hours with heating and cooling rates of 3°C.min^{-1}. The densities of the final pellets all reached over 92% of calculated density.

From each sample, one of the produced pellets was ground then characterized by EDS, XRD and μ-Raman, using previously detailed apparatus and protocols[10]. No significant difference in the chemical composition and structure was noted between the initial powdered mixed-oxides and the sintered pellets[10]. The mixed-oxides lattice parameters were refined from powder diffraction profiles using a profile matching procedure (Le Bail method) implemented in the Fullprof suite software [19] while the sizes of the coherent domains (crystallite size) were estimated thanks to the Sherrer formula.

The dissolution experiments were performed using a similar protocol than that used for dissolution experiments of powdered samples[13,14]. Briefly, polytetrafluoroethylene (PTFE) vials were selected on the basis of their low adsorption properties regarding the studied elements. For each experiment, the powdered sample or the pellet was placed in a sealed vial with a precise volume of 20 or 30 mL of 4M HNO_3 (prepared from an analytical grade solution) then placed in an oven at 60 or 90°C.

Regular uptakes of the solution were performed to determine the rare earth elements (REE) releases. These concentrations were determined using a Spectro Arcos EOP ICP-AES apparatus, which was daily calibrated using ICP standard solution (SPEX) of each element.

The comparison of the samples was performed using the normalized weight losses[20], noted N_L, and expressed in g.m^{-2}. It was calculated from the determined elementary concentration after normalization by the weight ratio of the element i considered in the solid (f_i, g.g^{-1}), and by the reactive surface area of the sample contacted with the solution (S) (expressed in m[2]). As a first approximation, the latter was usually considered to be constant during the dissolution experiment. $N_L(i)$ values were thus calculated considering the following equation:

$$N_L(i) = \frac{m_i}{f_i \times S} \tag{1}$$

where m_i (expressed in g) corresponds to the amount of the element i measured in the solution. Derivating Eq. (1) as a function of dissolution time (t) led to the normalized dissolution rate of the element i ($R_L(i)$, expressed in $g.m^{-2}.d^{-1}$) as follows:

$$R_L(i) = \frac{d\,N_L(i)}{d\,t} = \frac{1}{f_i \times S} \times \frac{d\,m_i}{d\,t} \tag{2}$$

When the normalized dissolution rates determined for all the constitutive elements are close (typically for congruence ratio, $r = R_L(i)/R_L(j)$ ranging between 1/3 and 3)[21], the reaction of dissolution was called to be congruent*. In this case, the solid dissolution could be presented indifferently from the release of any of each constitutive element measured in solution.

On the contrary, if at least one of the elements selectively precipitates in a new solid phase in the back-end of the initial reaction of dissolution, the dissolution then appears to be incongruent[20]. Likewise, a true incongruent dissolution could be observed when at least one element is selectively released by the material.

In order to monitor the material dissolution with a good accuracy, the reactive surface S has to be determined as precisely as reasonably achievable. While this latter is easily obtained for powdered samples by the specific surface area measurement by N_2 or Kr adsorption using the BET method, it is difficult to transpose to a well densified sintered pellet. The use of such method requires the simultaneous analysis of numerous pellets, which appears experimentally restrictive[22]. Similarly, the evaluation of the reactive surface through geometric measurement (10^{-7} to 10^{-6} $m^2.g^{-1}$) is not satisfying since the values obtained from this method are usually several orders of magnitude lower than that formally identified in literature for dense ceramic objects based on krypton adsorption[22]. In order to get the better evaluation of the reactive surface samples, a method based on SEM observations of the pellet surfaces was developed. This method allowed the estimation of the surface area of the pores. It was mainly based on the assumption that the pore depth was equal to their diameter, as already described[23]. Then, the obtained area was considered as the reactive surface area of the solid/solution interface. Even though one can not exclude any deviation between the evolving surface examined at the micrometer scale and that of the entire solid, the direct comparison of dissolution of a large variety of materials including sintered pellets with various densification rates and powders with various specific surface areas led to consistent results. Some details regarding to this methodology will be described soon. The specific surface area of the studied samples were evaluated from micrographs recorded with a FEI Quanta 200 environmental scanning electron microscope. The values are listed in Table 1.

---

* In this sense, the term "congruent" differs from the thermodynamic meaning usually employed in the description of phase diagrams.

The same SEM device was also employed to follow the microstructural evolution of the pellets during their dissolution in nitric acid media. In order to proceed to such monitoring, the experiments were performed under several hundred Pa of water atmosphere. This ESEM mode hence appeared to be very convenient to preserve the solid/liquid interface (*e.g.* interfacial hydrated layers) that would

5 assuredly be degraded under vacuum conditions.

For each *in operando* observation of the pellets surface, it is mandatory to prevent the presence of HNO_3 in the SEM chamber, as its vapor could corrode and damage the inner walls, the final lenses and the detectors of the apparatus. Moreover, the presence of HNO_3 during the pumping sequence could also induce the formation of nitrate salt at the sample surface. In order to avoid such problems, the

10 considered pellets were first roughly dried by contacting both pellets sides on a soft absorbent towel, then by immersing the pellets few seconds in three successive beakers filled with deionized water. The sample was then immediately disposed on a flat stainless steel sample holder in the SEM chamber. To clean the atmosphere in the SEM, five cycles of gaseous water filling between 400 and 1000 Pa were programmed. ESEM observations of the pellets were then performed under water pressure ranging

15 from 250 to 400 Pa. Several locations of the samples surface were observed in order to ensure the homogeneity of their evolution during dissolution tests. Only the most representative were selected to be presented in this work. After the ESEM characterization, the pellet was brought back in the dissolution vial to continue the dissolution experiment.

20 **Table 1.** Composition, estimated specific surface area and relative density of the sintered samples.

Targeted composition	Obtained composition (EDS)	Specific surface area ($m^2.g^{-1}$)	Relative density* (%)
$Ce_{0.70}Nd_{0.30}O_{1.85}$	$Ce_{0.72}Nd_{0.28}O_{1.86}$	0.013	92%
$Ce_{0.40}Nd_{0.60}O_{1.70}$	$Ce_{0.41}Nd_{0.59}O_{1.705}$	0.01	95%
$Ce_{0.20}Nd_{0.80}O_{1.60}$	$Ce_{0.24}Nd_{0.76}O_{1.62}$	0.01	-
$Ce_{0.70}Er_{0.30}O_{1.85}$	$Ce_{0.71}Er_{0.29}O_{1.855}$	0.05	92%

* The given relative densities correspond to the ratio between the geometrical and the calculated densities. Reciprocally, it gives some insights of the global (i.e. open and closed) porosity within the pellets.

C Dissolution experiments

Considering the low reactive surface of sintered pellets, and the previous works done with powdered samples[13], dissolution tests were performed in 4M HNO_3 at 90°C in order to reach the quantitative dissolution of the ceramics within few weeks/months for the $Ce_{0.72}Nd_{0.28}O_{1.86}$ and $Ce_{0.71}Er_{0.29}O_{1.855}$ samples. Similarly, as the normalized dissolution rates of $Ce_{1-x}Ln_xO_{2-x/2}$ material in nitric media are expected to drastically increase with the neodymium incorporation rate[13], the temperature of the nitric acid media was reduced to 60°C in order to slow down the reaction of dissolution for $Ce_{0.41}Nd_{0.59}O_{1.705}$ and $Ce_{0.24}Nd_{0.76}O_{1.62}$.

C.1 Dissolution of $Ce_{0.72}Nd_{0.28}O_{1.86}$ and $Ce_{0.71}Er_{0.29}O_{1.855}$

The evolutions of the normalized weight losses (N_L) obtained during the dissolution of $Ce_{0.72}Nd_{0.28}O_{1.86}$ and $Ce_{0.71}Er_{0.29}O_{1.855}$ sintered samples in 4M HNO_3 at 90°C are viewed in Fig. 1. For both experiments, a congruent dissolution behavior was noted as Ce and Nd (or Er) were released in solution with similar N_L values. Besides, linear increases of the normalized weight losses (N_L) as a function of the dissolution time were also evidenced for the first 5 to 10% of dissolved materials. The associated initial normalized dissolution rates reached $R_{L,0}(Ce) \approx R_{L,0}(Nd) = (1.8 \pm 0.2) \times 10^{-1}$ $g.m^{-2}.d^{-1}$ and $R_{L,0}(Ce) \approx R_{L,0}(Er) = (7.7 \pm 0.8) \times 10^{-3}$ $g.m^{-2}.d^{-1}$) for $Ce_{0.72}Nd_{0.28}O_{1.86}$ and $Ce_{0.71}Er_{0.29}O_{1.855}$, respectively. In these conditions, the normalized dissolution rate of the Nd-based sample was thus about 20 times faster than the Er-based one. This trend was also observed on powdered samples[13,24]. It thus confirmed that the lighter the trivalent lanthanide element in $Ce_{1-x}Ln_xO_{2-x/2}$, the lower the chemical durability of samples in acidic media[13,14]. As already described, this latter tendency could result not only from the higher cohesion energy of the fluorite-type structure involving heavy rare earth elements, but also from some modifications of the constant associated to the nitrate complexation of lanthanides elements (higher values being obtained for the lighter lanthanide elements)[13,14,25].

The most relevant micrographs recorded during the ESEM monitoring of the two dissolution experiments are presented in Fig. 2 for $Ce_{0.72}Nd_{0.28}O_{1.86}$ and in Fig. 3 for $Ce_{0.71}Er_{0.29}O_{1.855}$. Up to 21 days for $Ce_{0.72}Nd_{0.28}O_{1.86}$ (~5% of the pellet leached) and 182 days for $Ce_{0.71}Er_{0.29}O_{1.855}$ (~7% of the pellet leached), the exact same locations were retrieved for each ESEM observation, in order to follow more precisely and efficiently the evolution of parameters such as roughness, intergranular distances, grain size, etc.
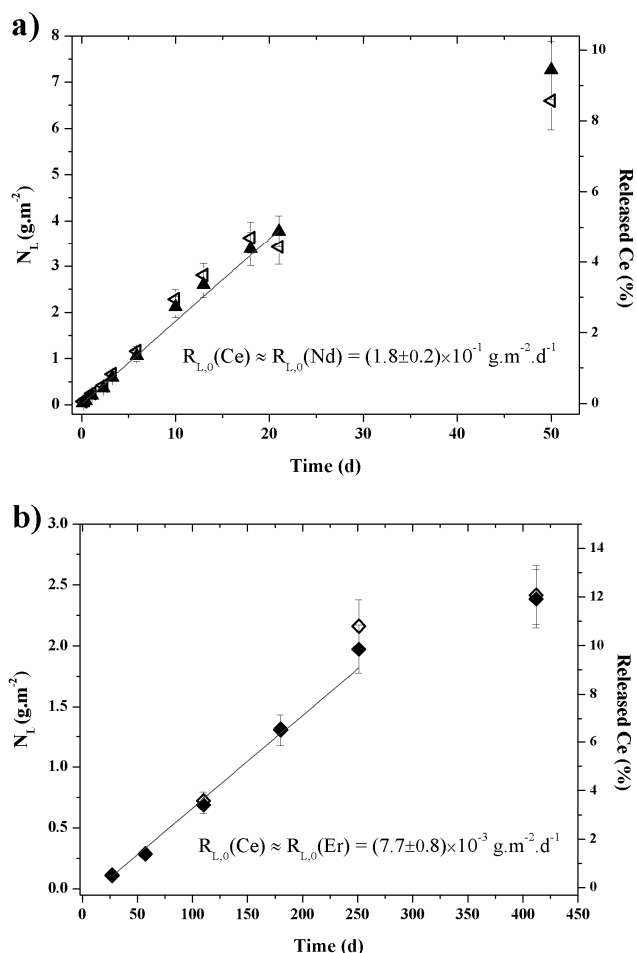
Fig. 1. Normalized weight losses (N_L) and corresponding dissolved fraction obtained during the dissolution of sintered pellets of $Ce_{0.72}Nd_{0.28}O_{1.86}$ **(a)** and $Ce_{0.71}Er_{0.29}O_{1.855}$ **(b)** during their dissolution at 90°C in 4M HNO_3.
5 The filled symbols correspond to $N_L(Ce)$ while the empty ones are associated to $N_L(Nd)$ and $N_L(Er)$.

The most relevant micrographs recorded during the ESEM monitoring of the two dissolution experiments are presented in Fig. 2 for $Ce_{0.72}Nd_{0.28}O_{1.86}$ and in Fig. 3 for $Ce_{0.71}Er_{0.29}O_{1.855}$. Up to 21 days for $Ce_{0.72}Nd_{0.28}O_{1.86}$ (~5% of the pellet leached) and 182 days for $Ce_{0.71}Er_{0.29}O_{1.855}$ (~7% of the
10 pellet leached), the exact same locations were retrieved for each ESEM observation, in order to follow more precisely and efficiently the evolution of parameters such as roughness, intergranular distances, grain size, etc.
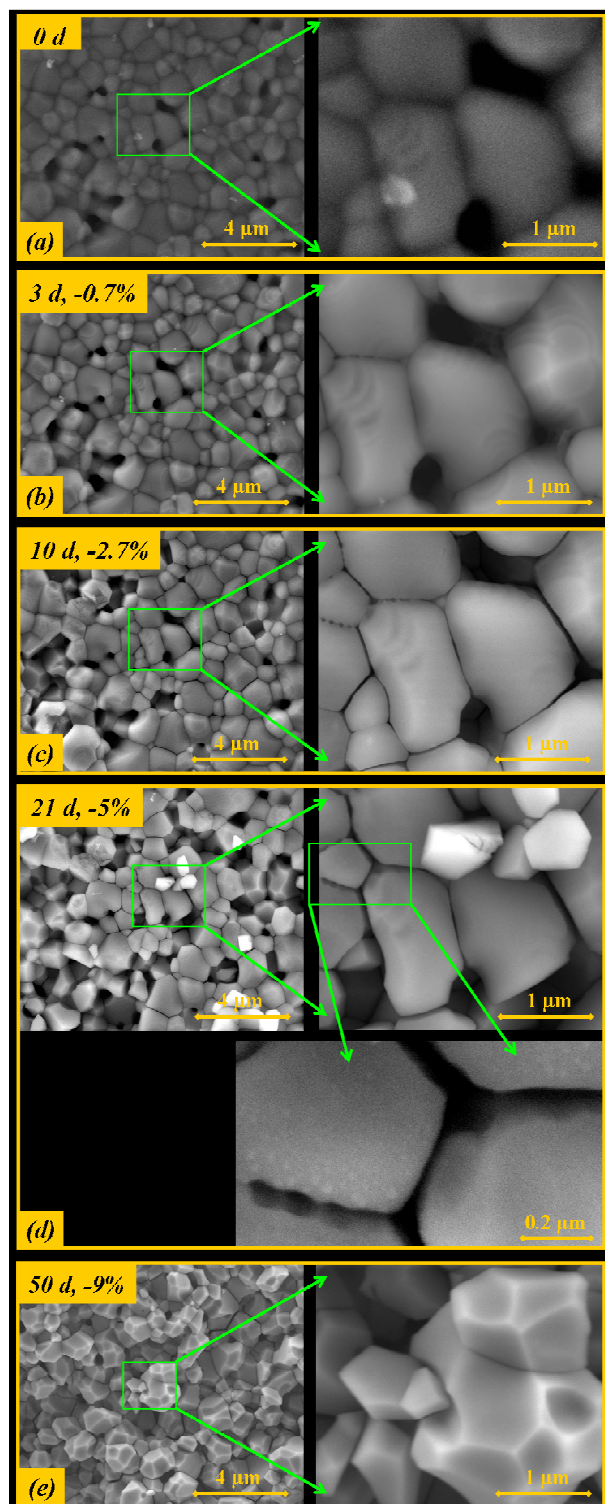
Fig. 2. ESEM observations (excepted for t = 0, high vacuum conditions) of the same zone of the $Ce_{0.72}Nd_{0.28}O_{1.86}$ samples surface during dissolution tests in 4M HNO_3 at 90°C. The percentages reported correspond to the mass fraction of dissolved material. The analyzed area remained the same during the dissolution experiments from 0 to
5 21 days and was representative of the overall sample.
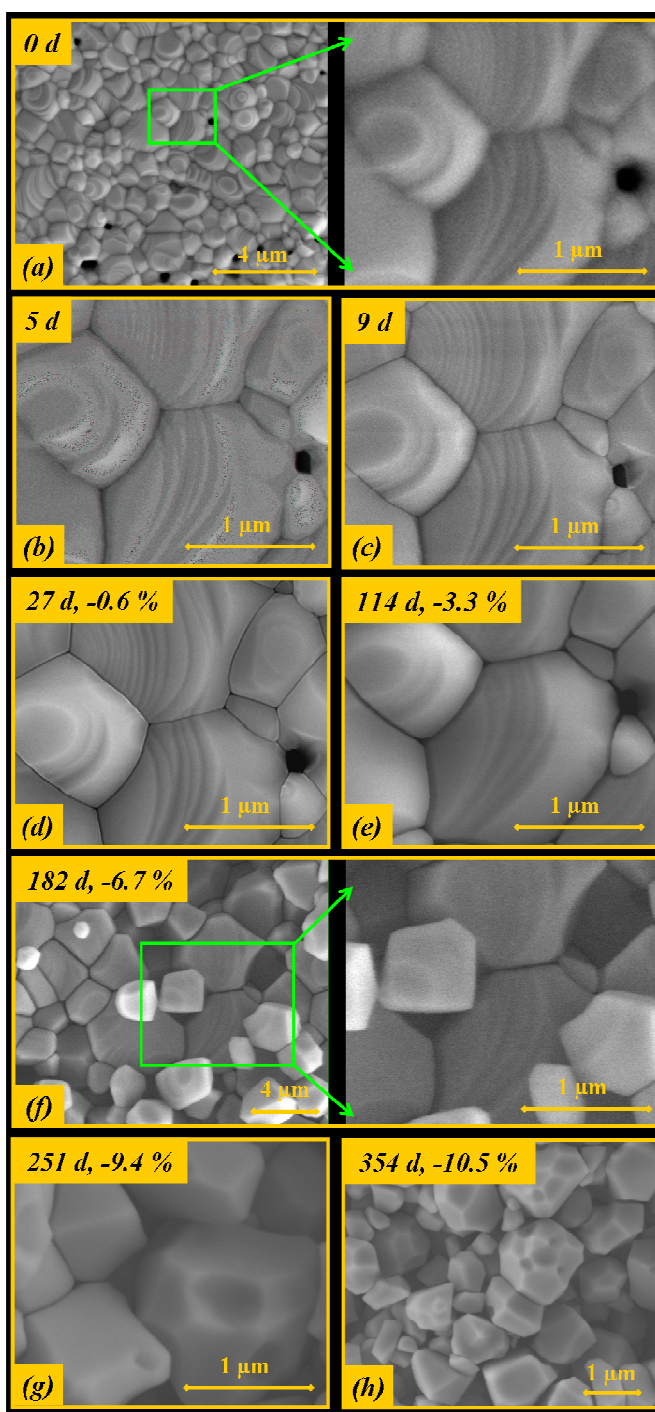
Fig. 3. ESEM observations (excepted for t = 0, high vacuum conditions) of the $Ce_{0.71}Er_{0.29}O_{1.855}$ samples surface during dissolution tests in 4M HNO_3 at 90°C. The percentages reported correspond to the mass fraction of dissolved material. The analyzed area remained the same during the dissolution experiments from 0 to 182 days and was representative of the overall sample.

The microstructure of the raw samples were both characteristic of well-sintered pellets since well-defined grain boundaries were clearly observed and only residual porosity was present[26]. The grain sizes ranged from 0.2 to 2 µm while the average crystallite size stands around 200 nm, thus indicating that each grain was generally constituted by a large amount of crystallites[24].

During the first days of dissolution (10 days for $Ce_{0.72}Nd_{0.28}O_{1.86}$ and 27 days for $Ce_{0.71}Er_{0.29}O_{1.855}$), no outstanding modification of the pellets topology was noted although a progressive digging of the grain boundaries was clearly evidenced. The most relevant example concerns the observation of $Ce_{0.71}Er_{0.29}O_{1.855}$ pellet after 9 days of dissolution. Indeed, during this early time the dissolution progression did not exceed 0.2% of the total material on the basis of ICP-AES results, while ESEM micrographs unambiguously evidenced that the material dissolution is essentially located within the grain boundaries. This clearly demonstrates that the grain boundaries constitute preferential dissolution zones, thus confirming several observations made on other ceramics[17,22,27]. This weaker chemical durability could stem from two characteristics of the grain boundaries:

- On the one hand, the chemical composition at the surface of a grain and, by analogy, at the grain boundaries, is often reported to be quite different than the bulk composition[28]. As instance, while the prepared samples appear homogeneous and single phase, a partial segregation of the Ln^{III} cation at grains surface can not be fully excluded. It was indeed already reported in $Ce_{1-x}Ln_xO_{2-x/2}$ materials[17,29-32]. As the chemical durability of $Ce_{1-x}Ln_xO_{2-x/2}$ strongly depends on the trivalent element content within the solid (an increase by one order of magnitude of dissolution kinetics being observed each 9 mol% of Ln^{III} incorporated in the structure)[13,14], this chemical segregation, even though limited, could induce a local enhancement of the dissolution process.

- On the other hand, grain boundaries are defined in ceramics as a junction between two grains and they correspond to a concentration of crystal defects. It usually lead to the formation of an intermediate thin layer (few nanometers) presenting a degraded crystalline order or even an amorphous state[28,33,34]. This implies a strong decrease of the cohesion energy [28,35]. Consequently, the energy required to remove the atoms coming from grain boundaries is expected to be lower than in the grain. This could explain the preferential dissolution observed[36].

In order to follow the evolution of grain boundaries digging, the average width between two grains was determined on each ESEM image at high magnification for $Ce_{0.71}Er_{0.29}O_{1.855}$. The evolution of intergranular width is shown in Fig. 4. It clearly underlines a two-step regime in the dissolution within the grain boundaries. Indeed, for t < 9 days, the intergranular width sharply increases to about 10 nm (*i.e.* rate of 1 nm.d^{-1}), which appears consistent with the thickness of the impaired crystalline order commonly reported in litterature[28] and that of the trivalent element enriched layer[29]. For longer

dissolution times, a second regime (about seven times slower, ~0.15 nm.d^{-1}) is established and likely corresponds to the dissolution of the $Ce_{0.71}Er_{0.29}O_{1.855}$ bulk material.

This assumption was confirmed through ESEM observations. Indeed over 3 days for $Ce_{0.72}Nd_{0.28}O_{1.86}$ and 9 days for $Ce_{0.71}Er_{0.29}O_{1.855}$, the dissolution of the grains boundaries seems not to rule the overall

5 dissolution mechanism and the contribution of the grains surface dissolution becomes predominant. This is particularly evidenced for the $Ce_{0.71}Er_{0.29}O_{1.855}$ experiment through the progressive and homogeneous disappearance of the initial grain surface ridges between 9 and 182 days (Fig. 3c to f).

From 10 days for $Ce_{0.72}Nd_{0.28}O_{1.86}$ and 182 days for $Ce_{0.71}Er_{0.29}O_{1.855}$, the dissolution of grain boundaries and of the surface of the grains induces the breakaway of the first layers of grains. In the

10 meantime, two other phenomena are noticeable at the surface of the grains. First of all, white spots of about 10 nm near the edge of grains are clearly evidenced for t = 21 days during the dissolution of $Ce_{0.72}Nd_{0.28}O_{1.86}$ (Fig. 2d). These nanometric phases were most likely present for the other dissolution times during the dissolution of $Ce_{0.72}Nd_{0.28}O_{1.86}$ and $Ce_{0.71}Er_{0.29}O_{1.855}$ but due to their small size, they were hard to evidence by ESEM. They could correspond to neoformed phases due to the establishment

15 of some local saturation conditions at the solid/solution interface and/or to the first step of the formation of a gelatinous dissolution layer at the material surface[13,15,17,21,37]. Moreover, the grains shape appeared to be strongly modified by the dissolution process when near 10% of the $Ce_{0.72}Nd_{0.28}O_{1.86}$ and $Ce_{0.71}Er_{0.29}O_{1.855}$ pellets were dissolved (Fig. 2e and Figs. 3g and h). Indeed, the surface of the grains surface was heterogeneously hollowed out and led to the formation of that is

20 usually called "corrosion pits" by analogy with the term usually employed during the corrosion of metallic alloys[38-44]. These corrosion pits were more clearly observed during the dissolution of $Ce_{0.41}Nd_{0.59}O_{1.705}$ pellet as it will be discussed hereafter.
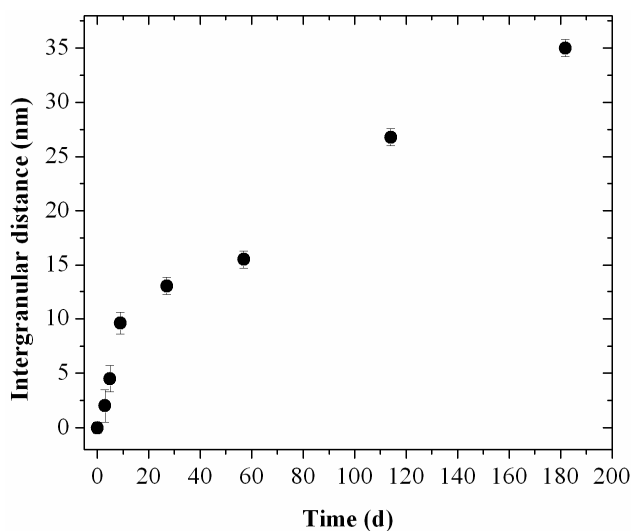
Fig. 4. Evolution of the average intergranular distance determined during the dissolution of $Ce_{0.71}Er_{0.29}O_{1.855}$ and obtained from ESEM

25 observations.

C.2 Dissolution of $Ce_{0.41}Nd_{0.59}O_{1.705}$

In order to study a less chemically-durable system, dissolution tests were performed on a sintered sample of $Ce_{0.41}Nd_{0.59}O_{1.705}$ mixed-oxide. Indeed, due to the higher neodymium content, the normalized dissolution of $Ce_{0.41}Nd_{0.59}O_{1.705}$ (Ia-3 space group, *i.e.* fluorite Fm-3m superstructure,
5 called bixbyite) is expected to be higher than for $Ce_{0.72}Nd_{0.28}O_{1.86}$. However, to get dissolution kinetics sufficiently slow to be experimentally handled but also to avoid the existence of diffusion kinetics that could result from the formation of neoformed phases, the temperature of the leaching 4M HNO_3 solution was reduced at 60°C. The studied pellet, whose initial microstructure is given in Fig. 5*a*, exhibited a high densification rate ($d_{mes.}/d_{cal.}$ = 95%) and was constituted of grains of 0.5 to 5 µm in
10 size. From the elemental releases in solution, the dissolution was checked to be congruent and led to normalized dissolution rates $R_{L,0}(Ce) = R_{L,0}(Nd) = 1.6\pm0.8$ g.m^{-2}.d^{-1} close to that obtained on powders in the same operating conditions (*i.e.* $R_{L,0} = 3.6\pm0.4$. g.m^{-2}.d^{-1})[13]. These close values underline the absence of strong effect of the sintering on the initial normalized dissolution rate for such poorly durable materials. It also confirms the relevant evaluation of the specific surface area on sintered
15 samples.

The results of ESEM monitoring of the $Ce_{0.41}Nd_{0.59}O_{1.705}$ dissolution are reported in Fig. 5. Similarly to what was observed for $Ce_{0.72}Nd_{0.28}O_{1.86}$ and $Ce_{0.71}Er_{0.29}O_{1.855}$ dissolution, the preferential dissolution of the grain boundaries was clearly evidenced (Fig. 5*b*). In the meantime, the formation of few corrosion pits was also noted (red-surrounded zones in Fig. 5*b*). The formation of these corrosion pits
20 thus began while less than 0.2% of the solid was dissolved. As a comparison, these pits were only evidenced for dissolution rate of at least 10% for $Ce_{0.72}Nd_{0.28}O_{1.86}$ and $Ce_{0.71}Er_{0.29}O_{1.855}$. Thus, the dissolution through corrosion pits seems to contribute earlier to the global dissolution when increasing the lanthanide incorporation rate in the structure and/or when the structure moved from the fluorite to the bixbyite superstructure.

25 The number and size of the pits regularly increase when extending the dissolution time. It is worth noting that their general shape moved progressively from hemispheric to pyramidal. Similar dissolution features were already reported during the dissolution of metallic alloys[42-44], oxides (notably fluorite-type materials[27,36,45-47]), and of natural minerals[46-52]. Considering the significant work of Pina et al. on phosgenite[52] and with the help of atomic force microscopy (AFM) observations, the obtained
30 corrosion pits shapes could be explained by two close, but notwithstanding different, mechanisms:

● The first and here mainly observed mechanism of corrosion pit formation and growing corresponds to the hemispheric then pyramidal-shape pits (Fig. 5*b* to *i*). As described in literature, hemispheric pits are usually formed from screw dislocation, *i.e.* a one-dimension crystalline defect

which goes through a straight line connecting the vertex and the center of the base of the final pyramid[52,53], thus explaining the trajectory of pit digging. The progressive transition of pyramidal shape pits could be further explained with the help of TSK (Terrace-Step-Kink) model[54,55]. This model is mainly based upon the principle that the energy required to remove an atom from the surface of a solid mainly depends on the number of bonds to other surface atoms that must be broken. According to that, the resistance to dissolution of a perfect plane surface, hence made of surface atom with 5 nearest neighbors is higher than a rounded surface which doubtlessly contains more kink or steps atoms (respectively 3 and 4 neighbors). As a consequence, the dissolution process contributes to the progressive evolving of hemispheric pits and thus to the formation of plane walls, *i.e.* pyramidal-shape pits.

• The secondary mechanism of corrosion pit formation and evolving here observed consists of initially very thin squares (height of few unit cells), whose development on the material surface is considerably quicker than the digging in the bulk material and whose formation is initiated from edge dislocation[53]. For the higher dissolution times, the stacking of these squares indirectly leads to the digging of these pits so well that they become observable by ESEM[45,50-52]. In the present study, such features were not observed before 150 hours, but they are clearly evidenced from this time and over. Among the presented micrographs, two of these pits could notably be seen in the left of Fig. 5*h*.
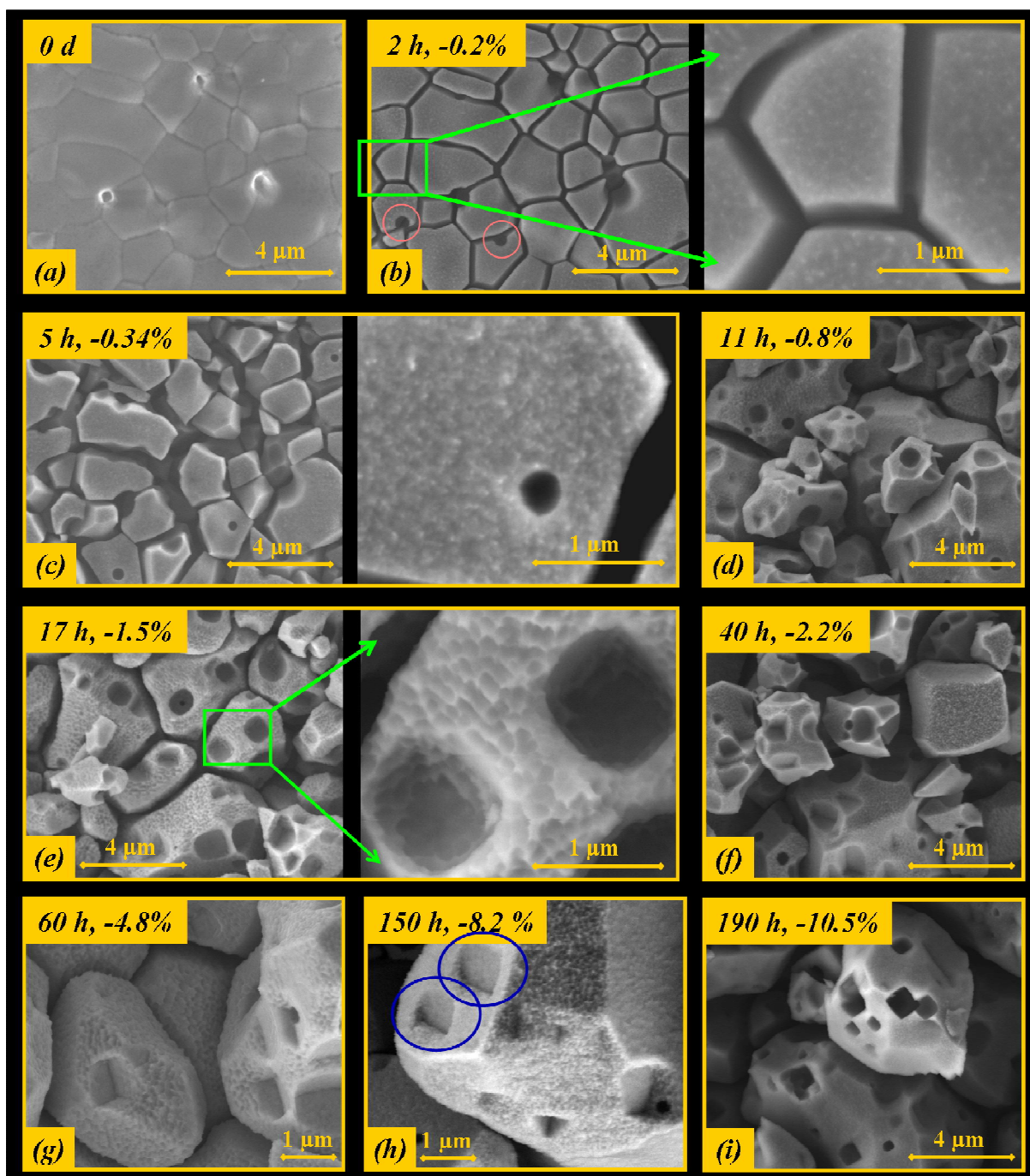
Fig. 5. ESEM observations (excepted for t = 0 d, high vacuum conditions) of the $Ce_{0.41}Nd_{0.59}O_{1.705}$ samples surface during its leaching in 4M HNO_3 at 60°C. Given percentages correspond to the solid dissolved fraction at the considered time. The significance of circled area is given in the text.

C.3 Dissolution of $Ce_{0.24}Nd_{0.76}O_{1.62}$

$Ce_{1-x}Nd_xO_{2-x/2}$ oxides were all found to be polyphasic for trivalent lanthanide substitution rates higher than 0.7 [10,56-58] : the first phase followed the C-type structure (bixbyite) with an associated chemical composition close to $Ce_{0.28}Nd_{0.72}O_{1.64}$. The second phase crystallized with an hexagonal A-type structure (characteristic of Nd sesquioxide) with a very low cerium incorporation rate. In order to underline the effects associated to the presence of less durable secondary phase on the chemical durability and microstructure evolution, sintered sample of $Ce_{0.24}Nd_{0.76}O_{1.62}$ was dissolved at 60°C in 4M HNO_3 [13,14]. The results of ESEM monitoring during the dissolution are reported in Fig. 6. The two first micrographs show the microstructure of the raw material which was for the major part composed of micrometric grains of the C-type phase, while stick-shape Nd_2O_3 phases were present along some of the C-type $Ce_{0.28}Nd_{0.72}O_{1.64}$ grain boundaries.

After only one minute of dissolution, all the Nd_2O_3 domains of the pellet surface were fully dissolved, while C-type grains were globally unaltered. Since the normalized dissolution rates associated to the powdered A-type samples is several order of magnitude faster than that of the C-type $Ce_{0.28}Nd_{0.72}O_{1.64}$ [13], such a microstructure evolving was clearly expected. After this first microstructure change, the surface of the pellet was moderately modified until 11 minutes of dissolution. The preferential dissolution of the grain boundaries was then evidenced from 25 minutes of dissolution.

From ICP-AES monitoring, the evolution of the trivalent lanthanide releases seemed to follow a slight exponential trend that appears different to that observed for other systems already described (Fig. 7*a*). As an example, less than 1% of the solid was dissolved after 11 minutes. It reached about 5% after 14 additional minutes. Moreover, the dissolution appears surprisingly congruent, which seems to come in contradiction with ESEM observations (Nd_2O_3 grains being fully dissolved after only 1 minute). However, it is important to remind that Nd_2O_3 was present as a minor phase in the mixture and that the C-type $Ce_{0.28}Nd_{0.72}O_{1.64}$ phase also contains 72 mol% of neodymium. In such conditions, the incongruence due to the preferential dissolution of Nd_2O_3 could be difficult to evidence since it only induces a small deviation between $N_L(Ce)$ and $N_L(Nd)$ values (small initial pulse in the Nd release).

For t = 25 min (Fig. 6*e*), a layer covering the entire pellet surface was easily evidenced. The white dots observed at high magnification in Fig. 6*b* (t = 1 min) could also correspond to the early stage of this neoformed layer. As the layer appears translucent, it presumably corresponds to a hydrated phase as already described during the dissolution of other ceramics in nitric acid media[20]. Moreover, the hypothesis of the formation of a Nd-enriched layer at the material surface was supported by already published X-ray reflectometry (XRR) and Grazing-Incidence XRD experiments on $Ce_{0.4}Nd_{0.6}O_{1.7}$ pellets submitted to dissolution[17].
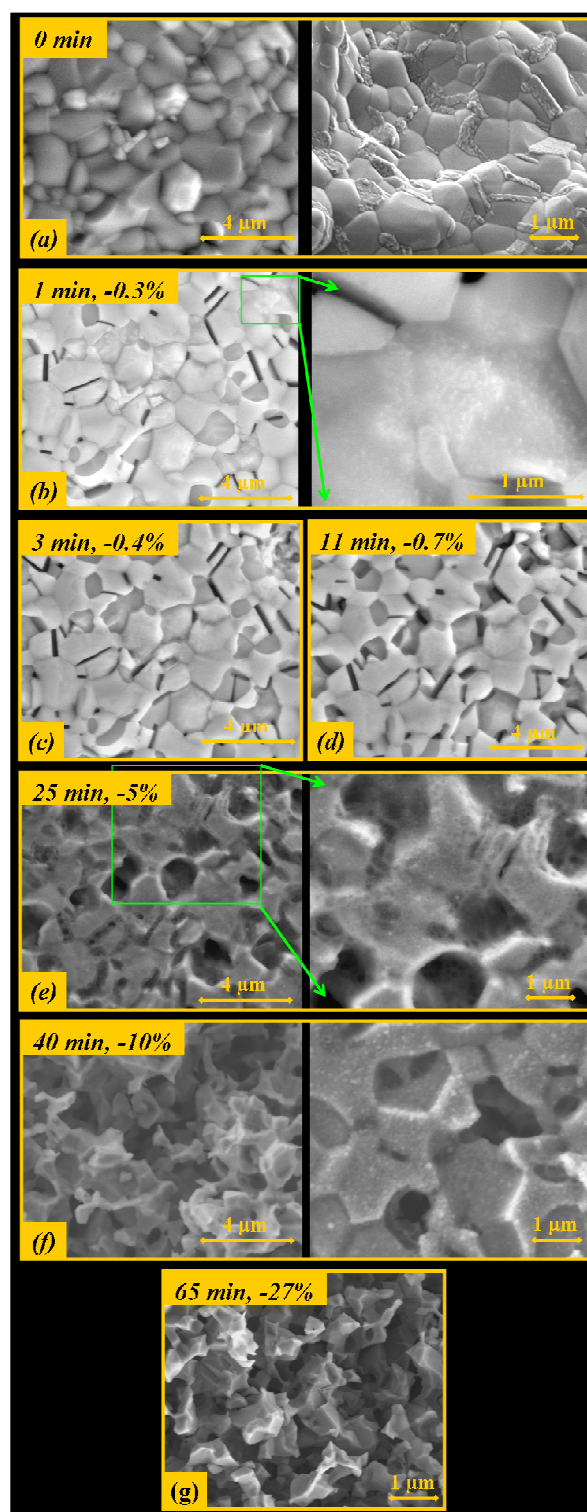
Fig. 6. ESEM observations of the $Ce_{0.24}Nd_{0.76}O_{1.62}$ biphasic sample during dissolution test at 60°C in 4M HNO_3. The percentages reported correspond to the ratio of dissolved material.

Similarly, the development of a hydrated phase during the dissolution of powdered $Ce_{0.72}Nd_{0.28}O_{1.86}$ was also evidenced (see section C.4). The existence of such phase was also supported by the evolution

of N_L generally obtained during the dissolution of $Ce_{1-x}Nd_xO_{2-x/2}$[13] powders in nitric acid solutions. Indeed a progressive slowing down of the normalized dissolution rates by one order of magnitude was often observed and assigned to the existence of diffusion phenomena at the solid/liquid interface.

Moreover, the exponential evolution of N_L (Fig. 7a) was mainly assigned to an important increase of the reactive surface area S with the progress of the dissolution reaction. Indeed, the preferential dissolution of the grain boundaries and of the Nd_2O_3 phase for $Ce_{0.72}Nd_{0.28}O_{1.86}$ allows the solution to quickly penetrate the inner material . As a consequence, at t = 25 min, the pellet became percolant and crumbled into a powder when handled for t = 65 min (Fig. 6g). In order to evidence then quantify this reactive surface area increase, its evolving was evaluated during dissolution then determined by Kr-absorption (BET method) when possible, *i.e.* for the longer leaching times (Table 2). We checked that the values obtained from SEM images examinations during the first 11 minutes of dissolution were in good agreement with that experimentally measured over 40 min.

Table 2. Evolution of the specific surface area during the dissolution of $Ce_{0.24}Nd_{0.76}O_{1.62}$ sintered sample in 4M HNO_3 at 60°C.

Dissolution time (min)	Specific surface area (m^2.g^{-1})	Determination method
0	0.01	SEM images analysis
1	0.10	SEM images analysis
3	0.15	SEM images analysis
11	0.2	SEM images analysis
40	0.3±0.1	BET (Kr absorption)
65	0.3±0.1	BET (Kr absorption)

The initial specific surface area, determined from SEM images analysis was estimated to 0.01 m^2.g^{-1} that appears consistent with the values usually reported for well-densified ceramics[22,23]. With the same method, the specific surface area increased by one order of magnitude (*i.e.* 0.1 m^2.g^{-1}) after only 1 minute of leaching due to the development of surface porosity and rugosity consequently to the quasi-instantaneous dissolution of the Nd_2O_3 grains initially present at the pellet surface. For higher dissolution times, the specific surface area increased more slowly (from 0.1 to 0.3 m^2.g^{-1}) than during the initial step. Above t = 40 min, the pellet became percolant. Thus, considering the higher specific surface area expected, this latter was determined by Kr-adsorption using the BET method with a Micromeritics ASAP 2020 apparatus. In order to preserve an eventual neoformed hydrated phase at the solid/liquid interface, the pellet was first dried and desorbed under soft conditions (90°C, ~0.1 mmHg). The obtained value ($S_{SA} = 0.3\pm0.1$ m^2.g^{-1}) was found to be consistent with that deduced from evaluation by ESEM. It remained almost constant when increasing the dissolution time up to 65 minutes.

The evolution of the normalized weight losses were thus corrected considering the specific surface area obtained (Fig. 7b). A quasi-linear evolution of $N_L(Ce)$ and $N_L(Nd)$ was then observed. It corresponded to normalized dissolution rates of $R_L(Nd) \approx R_L(Ce) = 1.4 \pm 0.7$ g.m^2.d^{-1} showing that the bias associated to the specific surface area evolving can be corrected by the evaluation of S_{SA} values during the dissolution experiments.
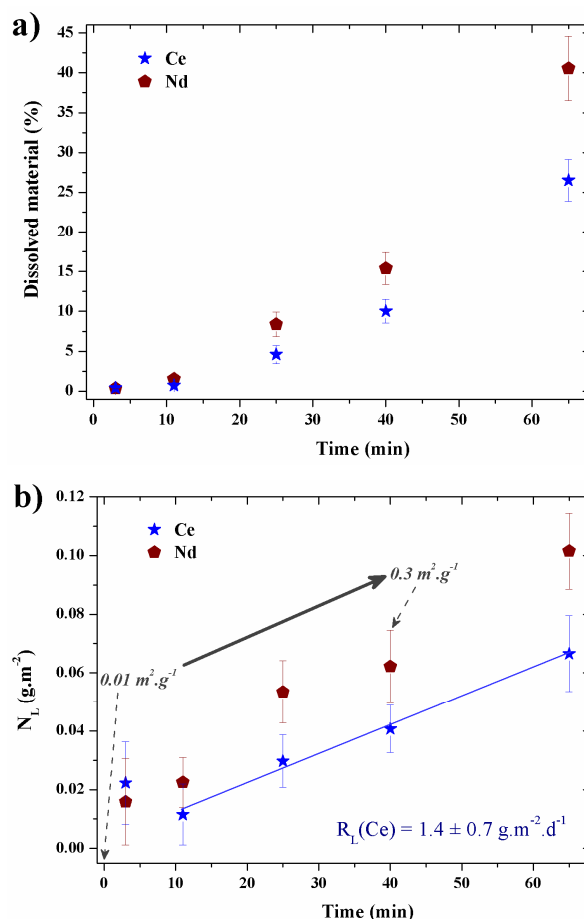
Fig. 7. Evolution of the dissolved material rate (a) and of the normalized weight loss $N_L(Ce)$ (★) and $N_L(Nd)$ (⬟) (b) observed during the dissolution of $Ce_{0.28}Nd_{0.72}O_{1.64}$ in 4M HNO_3 at 60°C determined considering the increase of the specific surface area during the dissolution (evaluation by ESEM or Kr-adsorption).

C.4 Comparison with powdered $Ce_{0.72}Nd_{0.28}O_{1.86}$ sample

The ESEM study was also applied to powdered $Ce_{0.72}Nd_{0.28}O_{1.86}$ heated at 1000°C then dissolved in 4M HNO_3 at 60°C. The kinetics of dissolution of such material was already described in a previously published paper[13]. With this purpose, five dissolution batches were put in contact with the solution for 3 h, 22 h, 3 d and 54 d then characterized by ESEM and BET (Table 3, Fig. 8). For making such characterization, the powders were separated from the solution by centrifugation at 4500 rpm then dried at 90°C. The same experiments were performed on powdered $Ce_{0.90}Nd_{0.10}O_{1.95}$. The results obtained were similar to that reported here after for $Ce_{0.72}Nd_{0.28}O_{1.86}$[24].

From Table 3, the specific surface area of the remaining material was found to increase rapidly during the first days of the experiment : from 3.5 ± 0.1 $m^2.g^{-1}$ for the starting powder up to 8.4 ± 0.2 $m^2.g^{-1}$ after only 3 h of dissolution (associated rate of dissolved material equal to 2%) and over 13.2 ± 0.2 $m^2.g^{-1}$ after 3 days (11% of dissolved material). Then, it slowly rose up to 15.4 ± 0.2 $m^2.g^{-1}$ after 21 days of dissolution.

This increase in the specific surface area was presumably mainly related to the progressive crumbling observed in Fig. 8. Indeed, the studied powder was initially constituted of slat-shape aggregates composed of hundreds of crystallites (Fig. 8*a*). When extending the dissolution time, the dissolution of the crystallites boundaries led to the quick crumbling of the aggregates which seemed to occur by successive crystallites layers breakaway as the slats thicknesses are found to decrease during the dissolution process (comparison of Fig. 8*a* and 8*e*). Throughout the experiment, the relative amount of single crystallites compare to the number of remaining aggregates increased significantly while the latter finally disappeared after only 50 days of dissolution (Fig. 8*f*), *i.e.* when about 25% of the solid was dissolved. Conversely, as the aggregates crumbling was almost completed after 21 days of dissolution, the associated specific surface area (*i.e.* 15.4 ± 0.2 $m^2.g^{-1}$) was found to be maximum in these dissolving conditions.

As observed for sintered $Ce_{0.72}Nd_{0.28}O_{1.86}$, the increase of specific surface area by almost a factor of 5 induced some bias in the normalized dissolution rate determination. In order to avoid this bias, all the data obtained were corrected considering the evolution of specific surface area. As expected, the corrected R_L values were noticeably lower than the former ones, as $R_{L,0}$ was equal to $(1.4\pm0.2) \times 10^{-3}$ $g.m^{-2}.d^{-1}$ (compared to $(7.1\pm0.7) \times 10^{-3}$ $g.m^{-2}.d^{-1}$). Even though the microstructural evolution and thus the specific surface area variation were found to be moderate for powders compared to highly densified pellets, the impact on the normalized dissolution kinetics appears significant and should be considered for rapid dissolution experiments. They could also contribute to the explanation of the role of "hidden parameters" as sometimes encountered in literature[59,60].

Moreover, the formerly evoked gelatinous layer was clearly evidenced for t = 3 d and 21 d (Fig. 8*d* and 8*e*). As already suggested, this neoformed layer acted as a diffusion barrier and was responsible for the slowing down of $Ce_{0.72}Nd_{0.28}O_{1.86}$ normalized dissolution rate by almost one order of magnitude, from $R_{L,0} = (1.4\pm0.2) \times 10^{-3}$ $g.m^{-2}.d^{-1}$ to $R_{L,t} = (1.3\pm0.4) \times 10^{-4}$ $g.m^{-2}.d^{-1}$, as reported previously[13].

Table 3. Evolution of the specific surface area of the undissolved part of the $Ce_{0.72}Nd_{0.28}O_{1.86}$ powder during its leaching in 4M HNO_3 at 60°C.

Time (d)	Specific surface area ($m^2.g^{-1}$)	Mass fraction of dissolved material (%)
0	3.5±0.1	-
0.13	8.4±0.2	2
0.9	10.9±0.2	6
3	13.2±0.2	12
8	13.9±0.2	15
21	15.4±0.2	22
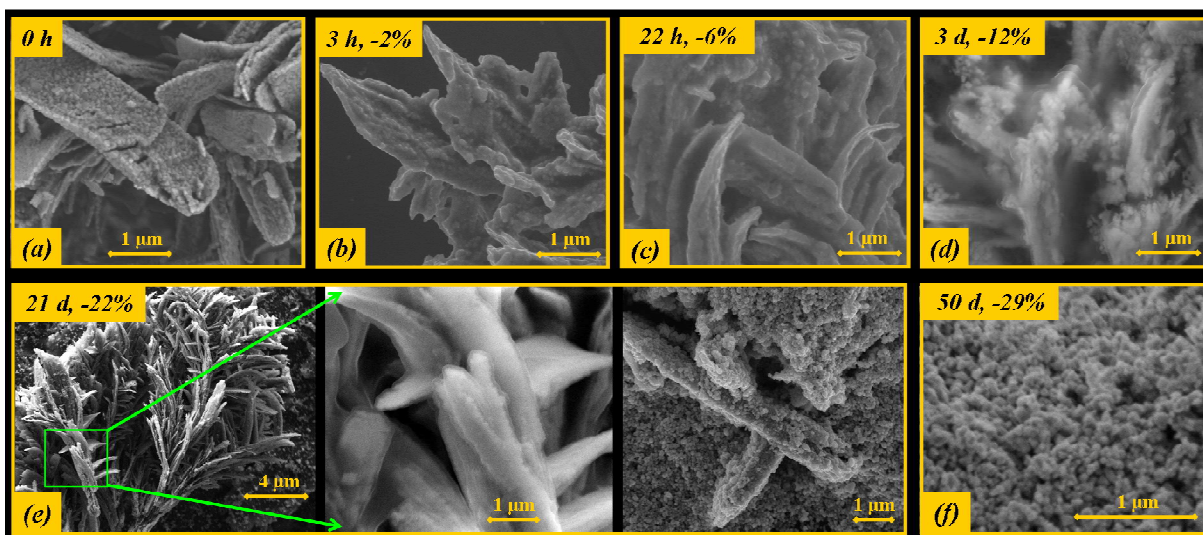
Fig. 8 ESEM observations of powdered $Ce_{0.72}Nd_{0.28}O_{1.86}$ sample during dissolution tests in 4M HNO_3 at 60°C. The percentages reported correspond to the mass fraction of dissolved material.

D Conclusion

The microstructural evolution of several $Ce_{1-x}Ln_xO_{2-x/2}$ sintered pellets during dissolution tests in 4M HNO_3 at 90°C or 60°C was examined as the first step of the better knowledge of the behavior of (spent) nuclear oxide fuels. Even though this kind of materials is not subjected to significant redox phenomena at the solid/solution interface contrarily to uranium based oxides, ESEM experiments were developed to follow the changes in the samples microstructure and their consequences on the dissolution evolution.

The main conclusions are summarized here after :

• As already described for several other ceramics, the preferential dissolution of grain boundaries was observed during the dissolution of $Ce_{1-x}Ln_xO_{2-x/2}$ sintered pellets. This relative weakness was mainly assigned to an impaired crystallinity compared to the bulk material and/or to a local trivalent lanthanide enrichment, as the Ln^{III} content was found to have one of the greatest influence on dissolution kinetics in these compounds. Grain boundaries thus contribute significantly to the initial step of the material dissolution.

• Crystalline defects, screw and edge dislocation, constitute the second kind of preferential dissolution zone evidenced in this study, as the formation and growth of corrosion pits, mainly of pyramidal shape, was observed overall the surface grains during the dissolution.

• The above-mentioned preferential dissolution modes (grain boundaries, crystalline defects) also indirectly induce significant and non-linear increase of the reactive surface developed at the solid/liquid interface.

• On sintered samples and even more clearly on powdered $Ce_{0.72}Nd_{0.28}O_{1.86}$ sample, the formation of a gelatinous layer resulting of processes occurring at the back-end of the dissolution process (*e.g.* local saturation of the leaching solution at the solid/solution interface), was evidenced through ESEM observations. This gel is also presumably responsible for normalized dissolution rate decreasing often reported in previous experiments performed for such powdered samples[13-16].

• The experiment concerning the biphasic $Ce_{0.24}Nd_{0.76}O_{1.62}$ sample pointed out that the presence of a secondary highly soluble phase (Nd_2O_3) is found to strengthen this specific surface area increase and the bias on the normalized dissolution rates. Such microstructural heterogeneity evidently disturb the determination of normalized dissolution rates.

From these observations, it appears that the kinetic study of a material dissolution can clearly benefit from the monitoring of the microstructure evolution and particularly that of reactive surface area.

However, it is important to note that for the $Ce_{1-x}Nd_xO_{2-x/2}$ studied samples and by extension for the formerly studied $Ce_{1-x}Ln_xO_{2-x/2}$[13] and $Th_{1-x}Ln_xO_{2-x/2}$[14], the disruptive effect induced by this microstructural evolution remains of second order compared to the strong effects associated to

chemical composition (particularly to the trivalent lanthanide incorporation rate), temperature and acidity. Nevertheless, it should be considered carefully prior making the multiparamteric kinetics of dissolution in order to precise the accurate role of other studied conventional parameters. This aspect will become of strong interest when considering the dissolution of real (spent) nuclear fuels, as recently suggested in literature [60].

Acknowledgments

References

1   D. C. Crawford, D. L. Porter and S. L. Hayes, *J. Nucl. Mater.*, 2007, **371**, 202.

2   M. K. Meyer, R. Fielding and J. Gan, *J. Nucl. Mater.*, 2007, **371**, 281.

3   K. Tucek, J. Carlsson and H. Wider, *Nucl. Eng. Des.*, 2006, **236**, 1589.

4   D. Warin, *J. Nucl. Sci. Technol.*, 2007, **44**, 410.

5   Y. Zhang, J. Wallenius and A. Fokau, *Annals Nucl. Energ.*, 2010, **37**, 629.

6   C. W. Forsberg, P. F. Peterson and P. S. Pickard, *Nucl. Tech.*, 2003, **144**, 289.

7   D. LeBlanc, *Nucl. Eng. Des.*, 2010, **240**, 1644.

8   *Comprehensive Nuclear materials*, Ed.-in-chief R. J. M. Konings, Elsevier, Amsterdam, 2012, vol. 1: *Advanced Fuels/Fuel Cladding/Nuclear Fuel Performance Modeling and Simulation*.

9   DoE, U.S., *A technology roadmap for generation IV nuclear energy systems*, Generation IV International Forum, 2002.

10 G. Heisbourg, S. Hubert, N. Dacheux and J. Purans, *J. Nucl. Mater.* 2004, **335**, 5.

11 G. Heisbourg, S. Hubert, N. Dacheux and J. Ritt, *J. Nucl. Mater.* 2003, **321**, 141.

12 D. Horlait, L. Claparède, N. Clavier, S. Szenknect, N. Dacheux, J. Ravaux and R. Podor, *Inorg. Chem.*, 2011, **50**, 7150.

13 D. Horlait, N. Clavier, S. Szenknect, N. Dacheux, and V. Dubois, *Inorg. Chem.*, 2012, **51**, 3868.

14 D. Horlait, F. Tocino, N. Clavier, N. Dacheux and S. Szenknect, *J. Nucl. Mater.*, 2012, **429**, 237.

15 L. Claparède, N. Clavier, N. Dacheux, A. Mesbah, J. Martinez, S. Szenknect and P. Moisy, *Inorg. Chem.*, 2011, **50**, 11702.

16 L. Claparède, N. Clavier, N. Dacheux, P. Moisy, R. Podor and J. Ravaux, *Inorg. Chem.*, 2011, **50**, 9059.

17 S. Szenknect, A. Mesbah, D. Horlait, N. Clavier, S. Dourdain, J. Ravaux and N. Dacheux, *J. Phys. Chem. C*, 2012, **116**, 12027.

18 G. T. Seaborg, *Radiochim. Acta*, 1993, **61**, 115.

19 J. Rodriguez-Carvajal, *Physica B* 1993, **192**, 55.

20 A. C. Thomas, N. Dacheux, P. Le Coustumer, V. Brandel and M. Genet, *J. Nucl. Mater.* 2000, **281**, 91.

21 N. Dacheux, N. Clavier and J. Ritt, *J. Nucl. Mater.* 2006, **349**, 291-303.

22 N. Clavier, N. Dacheux, P. Martinez, E. Du Fou de Kerdaniel, L. Aranda and R. Podor, *Chem. Mater.*, 2004, **16**, 3357.

23 N. Dacheux, B. Chassigneux, V. Brandel, P. Le Coustumer, M. Genet and G. Cizeron, *Chem. Mater.*, 2002, **14**, 2953.

24 D. Horlait, Ph.D. Thesis, Université Montpellier 2, 2011, available at http://tel.archives-ouvertes.fr/tel-00769666.

25 A. Ruas, P. Moisy, J. P. Simonin, O. Bernard, J. F. Dufrêche, P. Turq, *J. Phys. Chem. B*, 2005, 109, 5243

26 M. N. Rahaman, Ceramic processing and sintering, Marcel Dekker, New-York, 1995.

27 J. R. A. Godinho, S. Piazolo and L. Z. Evins, *Geochim. Cosmochim. Acta*, 2012, **86**, 392.

28 L. Priester, *Grain Boundaries, From Theory to Engineering*, Springer, 2013.

29 Y. Lei, Y. Ito, N. D. Browning and T. J. Mazanec, *J. Am. Ceram. Soc.*, 2002, **85**, 2359.

30 M.-F. Luo, Z.-L. Yan, L.-Y. Jin and M. He, *J. Phys. Chem. B*, 2006, **110**, 13068.

31 V. Bellière, G. Joorst, O. Stephan, F. M. F. de Groot and B. M. Weckhuysen, *J. Phys. Chem. B*, 2006, **110**, 9984.

32 Z.-P. Li, T. Mori, G. J. Auchterlonie, J. Zou and J. Drennan, *Appl. Phys. Lett.*, 2011, **98**, 093104.

33 D. Wolf, *Curr. Opin. Solid. St. M.*, 2001, 5435.

34 N. Thangaraj and U. Dahmen, MRS proceedings, 1992, **238**, 171.

35 J. C. Conesa, *Surf. Sci.*, 1995, **339**, 337.

36 L. Claparede, F. Tocino, S. Szenknect, A. Mesbah, N. Clavier, P. Moisy and N. Dacheux., *Inorg. Chem.*, submitted.

37 W. Stumm, Chemistry of the solid-water interface, Wiley, New-York, 1992.

38 B. Malki and B. Barroux, *Corr. Sci.* 2005, **47**, 171.

39 S.-T. Myung , Y. Hitoshi and Y.-K. Sun, *J. Mater. Chem.*, 2011,**21**, 9891.

40 K. S. Eom, J. Y. Kwon, M. J. Kim and H. S. Kwon, *J. Mater. Chem.*, 2011, **21**, 13047.

41 T. Nagatani, *Phys. Rev. Lett.*, 1992, **68**, 1616.

42 T. Martin and K. R. Hebert, *J. Electrochem. Soc.*, 2001, **148**, B101.

43 J. E. Castle and R. Ke, *Corros. Sci.*, 1990, **30**, 409.

44 M. Baumgärtner and H. Kaesche, *Corros. Sci.*, 1990, **31**, 231.

45 J. Romer, M. Plaschke, G. Beuchle and J. I. Kim, *J. Nucl. Mater.*, 2003, **322**, 80.

46 K. Sangwal and S. K. Arora, *J. Mater. Sci.*, 1978, **13**, 1977.

47 J.-M. Gautier, E. H. Oelkers and J. Schott, *Geochim. Cosmochim. Acta*, 2001, **65**, 1059.

48 G. Jordan, S. R. Higgins, C. M. Eggleston, K. G. Knauss and W. W. Schmahl, *Geochim. Cosmochim. Acta*, 2001, **65**, 4257.

49 G. Jordan, S. R. Higgins, C. M. Eggleston, S. M. Swapp, D. E. Janney and K. G. Knauss, *Geochim. Cosmochim. Acta*, 1999, **63**, 3183.

50 I. N. MacInnis and S. L. Brantley, *Chem. Geol.*, 1993, **105**, 31.

51 E. Ruiz-Agudo, C. V. Putnis, C. Jimenez-Lopez and C. Rodriguez-Navarro, *Geochim. Cosmochim. Acta*, 2009, **73**, 3201.

52 C. M. Pina, L. Fernandez-diaz, M. Prieto and A. Putnis, *Geochim. Cosmochim. Acta*, 2000, **64**, 215.

53 D. Hull and D. J. Bacon, *Introduction to dislocations*, Pergamon Press, 4th ed., 1984.

54 J. Villain, D. R. Grempel and J. Lapujoulade, *J. Phys. F*, 1985, **15**, 809.

55 K. Oura, V. G. Lifshits, A. A. Saranin, A. V. Zotov, M. Katayama and J. T. Yates, *Surface Science: An Introduction*, Springer-Verlag, Berlin, 2003

56 S. V. Chavan, M. D. Matthews and A. K. Tyagi, Mater. Res. Bull., 2005, **40**, 1558.

57 Y. Ikuma, E. Shimada and N. Okamura, *J. Am. Ceram. Soc.*, 2005, **88**, 419.

58 T. Hagiwara, Z. Kyo, A. Manabe, H. Yamamura and K. Nomura, *J. Ceram. Soc. Jpn.*, 2009, **117**, 1306.

59 J. Vandenborre, B. Grambow and A. Abdelouas, *Inorg. Chem.*, 2010, **49**, 8736.

60 H. Ikeuchi, A. Shibata, Y. Sano, T. Koizumi, *Proc. Chem.*, 2012, **7**, 77.